

# Vibrational Lifetimes and Spectral Shifts in Supercritical Fluids as a Function of Density: Experiments and Theory

D. J. Myers, Motoyuki Shigeiwa, and M. D. Fayer\*

Department of Chemistry, Stanford University, Stanford, California 94305

Binny J. Cherayil

Department of Inorganic and Physical Chemistry, Indian Institute of Science, Bangalore-560034, India

Received: August 2, 1999; In Final Form: December 14, 1999

Vibrational lifetime and spectral shift data for the asymmetric CO stretching mode of  $W(CO)_6$  in supercritical ethane, carbon dioxide, and fluoroform as a function of density at two temperatures are presented, and the lifetime ( $T_1$ ) measurements are compared to theory. The data and theory are refinements of previous work. Measurements at zero density allow the contribution from solute–solvent interactions to be separated from strictly intramolecular contributions to  $T_1$ . The results in the polyatomic SCFs are compared to data in Ar. The density functional/thermodynamic theory<sup>1</sup> has been extended to include contributions at large wavevector ( $k$ ). Very good, quantitative agreement between theory and data taken in ethane and fluoroform is achieved, but the agreement for data taken in carbon dioxide, while reasonable, is not as good. The theory uses a variety of input information on the SCF properties obtained from the fluids' equations of state and other tabulated thermodynamic data. The solute–solvent spatial distribution is described in terms of hard spheres. The theory is able to reproduce the data without solute–solvent attractive interactions or clustering in the calculation of the spatial distribution.

## I. Introduction

The vibrational lifetime ( $T_1$ ) of a mode of a polyatomic molecule in a polyatomic solvent is, in part, determined by the interactions of the internal degrees of freedom of the solute with the solvent.<sup>2–6</sup> If the solvent is a supercritical fluid (SCF), such as ethane, it is possible to examine the role of solute–solvent interactions in vibrational relaxation by changing the solvent density at fixed temperature. In this paper, we further consider the behavior of  $T_1$  of the asymmetric CO stretching mode of  $W(CO)_6$  ( $\sim 2000\text{ cm}^{-1}$ ) in supercritical ethane, fluoroform, and carbon dioxide ( $CO_2$ ) as a function of density from low density (well below the critical density) to high density (well above the critical density) at two temperatures, one close to the critical temperature and one significantly above the critical temperature.<sup>7</sup>  $T_1$  is measured using infrared (IR) pump–probe experiments. The vibrational absorption line positions as a function of density are also reported in the three solvents<sup>8</sup> at the two temperatures.

$T_1$  in a polyatomic molecule can arise from both intramolecular and intermolecular processes. To separate the solute–solvent intermolecular contributions to  $T_1$  from intramolecular vibrational relaxation, measurements of  $T_1$  at zero density are reported. While the IR pump–probe measurements of the vibrational relaxation in SCFs are all single exponential decays, the decay at zero density (pure gas-phase  $W(CO)_6$ ) is a triexponential.<sup>9</sup> The nature of the triexponential decay is briefly discussed so that the component corresponding to the zero density  $T_1$  can be used in the data analysis. In addition, measurements in Ar as a function of density show that  $T_1$  is density independent, in contrast to the density dependence observed in the polyatomic SCFs. Possible differences in solute–solvent interactions responsible for distinct behavior of  $T_1$  in polyatomic SCF solvents vs Ar are discussed.

As the experiments show,  $T_1$  is quite sensitive to solute–solvent interactions. There is considerable interest in the nature of solute–solvent interactions in SCFs, and a variety of experimental and theoretical techniques have been brought to bear on the subject.<sup>10–17</sup> Experimental work near the critical point often shows interesting anomalies. One of the ground-breaking studies<sup>16,17</sup> found that partial molal volumes of infinitely dilute solutes become large and negative in the compressible region around the critical point. Theoretical work<sup>18,19</sup> shows that these partial molal volumes should diverge to negative infinity at the critical point. Many different kinds of spectroscopic experiments have been performed on supercritical fluids. Absorption and/or fluorescence wavelengths often show a characteristic “three-regime” density dependence,<sup>11,20–22</sup> which will be discussed below. In addition, some studies<sup>23–25</sup> have observed greatly enhanced excimer emission near the critical point. Orientational motion has been studied near the critical point.<sup>26–28</sup> Some research shows that orientational motion slows down substantially,<sup>27</sup> though these results are debated by others.<sup>28</sup> Electron paramagnetic resonance experiments indicate that spin exchange and hyperfine coupling deviate from normal behavior near the critical point in some fluids.<sup>29,30</sup> Several excellent recent reviews have been written on these spectroscopic results.<sup>22,31</sup> Finally, X-ray and neutron scattering experiments done on supercritical fluids reveal the presence of large correlation lengths and long-range density fluctuations in the near-critical fluid.<sup>32,33</sup>

One of the fundamental questions involves the role of attractive solute–solvent interactions in SCFs. Strong solute–solvent attraction may give rise to enhanced local solvent density (solvent clusters) around a solute, particularly near the critical point.<sup>22,31,34,35</sup> It has been suggested that the formation of clusters

\* Corresponding author.

can account for anomalous experimental observations of solute properties in SCFs.<sup>22,31</sup> However, in connection with the vibrational relaxation experiments,<sup>8,36</sup> a theoretical approach was used that was based on the changing solvent properties to account for the density dependence of  $T_1$ , and attractive solute–solvent interactions were not part of the description of the solute/solvent spatial distribution.<sup>1</sup> The earlier version of the theory was based on an analysis limited to small wavevectors ( $k$ ) and was only able to describe the experimental data qualitatively. A scaling argument was used to suggest that, very near the critical point,  $T_1$  should be virtually density independent. Again, the scaling argument was based on a small  $k$  analysis. Simulations of vibrational relaxation in SCFs also suggest that no special solute–solvent interactions are necessary to account for the mild density dependence near the critical density.<sup>37</sup>

The results of the density dependent vibrational rate constant measurements are compared to a revised version of the theory. When the small  $k$  approximations were made, it was possible to obtain an analytical expression for the vibrational relaxation rate constant  $(1/T_1)^1$ . It has been pointed out that small  $k$  approximations are not appropriate.<sup>31,38</sup> Using numerical methods, we have now performed the calculations at all  $k$ . The form of the previously employed hydrodynamic equations has been modified so that they can be used at all  $k$ . Evaluation of the resulting theoretical expression shows good agreement with the  $T_1$  data in both ethane and fluoroform over a wide range of densities at two temperatures. Comparison of the theory and data in  $\text{CO}_2$ , while reasonable, seems to display a systematic deviation in the functional form of the theory compared to the data at high densities.

The theory involves parameters that are obtained from the SCF equations of state and other published data. Thus, detailed properties of solvent, including behavior near the critical point, are included in the theory. However, the solute and solvent spatial distribution is described in terms of hard spheres. An important point is that the theory is able to do a good job of reproducing the data without a description of the solute/solvent spatial distribution determined by solute/solvent attractive interactions that are stronger than the solvent/solvent interactions.

## II. Experimental Procedures

The laser system used to conduct the infrared pump–probe experiments on the asymmetric CO stretch of  $\text{W}(\text{CO})_6$  has been described previously.<sup>39,8</sup> Briefly, a Q-switched, mode locked, cavity dumped Nd:YAG laser is used to produce  $\sim 500 \mu\text{J}$  532 nm pulses ( $\sim 75$  ps fwhm) which provide the pump pulses in a  $\text{LiIO}_3$  OPA. The doubled output of the YAG laser also synchronously pumps a Rhodamine 610 dye laser. After amplification, the dye pulses ( $\sim 40$  ps fwhm) are  $\sim 30 \mu\text{J}$  at 595 nm. The dye pulses form the signal pulses in the OPA system. The typical output from the OPA is  $1.5 \mu\text{J}$  at  $\sim 5 \mu\text{m}$ . This power is sufficient to provide a detectable bleach in the  $\nu = 0-1$  transition but not enough to populate higher vibrational levels. The exact frequency of the infrared OPA is adjusted to overlap with the peak of the  $\text{W}(\text{CO})_6$  asymmetric ( $T_{1u}$ ) CO absorption, which changes somewhat with solvent, temperature, and density.

The samples were contained in a high-pressure cell which works well up to pressures exceeding 2500 psia. Sapphire or calcium fluoride windows provide an optical path for the counterpropagating pump and probe beams. Sample preparation has also been described previously.<sup>8</sup> Optical densities of the sample were usually 0.5–1.0, corresponding to  $\text{W}(\text{CO})_6$  concentrations of roughly  $10^{-5}$  mol/L. The experimental results did not show a dependence on solute concentration.

Two major changes have been made from the previous experimental setup. The first is that a small but finite pressure calibration error was corrected. During the previous experiments, the pressure transducer was misreading the pressure by  $\sim 10$  psia ( $\sim 0.67$  atm), a negligible error for the vast majority of reported experimental data.<sup>8,36</sup> However, near the critical density ( $\rho_c$ ) and temperature ( $T_c$ ), small pressure differences can create significant changes in the density. Thus, the densities calculated from the various equations of state were inaccurate for points in the immediate vicinity of  $(T_c, \rho_c)$ .

The second experimental improvement involves the method of heating and temperature controlling the sample. Previously, tubing and fittings connected to the cell were not temperature regulated at the same temperature as the cell. The presence of cold gas in the tubes connected to the cell produced very small inhomogeneities in density at temperatures and densities very near the critical point. A sensitive method was used to detect the problem. A collimated HeNe laser beam, with spot size small compared to the cell, was passed through the cell and examined at a long distance. When the beam was in line with the tubes, which are located on opposite sides of the cell, the beam appeared as if it had passed through a mild cylindrical lens. If the beam passed through the cell higher or lower, it was undistorted. Thus, the problem occurred in the center of the cell in line with the tubes. The distortion vanished if the density or temperature was changed so that the sample was not in proximity to the critical point. To obtain perfect uniformity, it was determined that everything connected to the cell needed to be at the same temperature, including tubes, valves, and the pressure transducer.

For thermodynamic measurements, the SCF cell is frequently immersed in a constant-temperature bath of a fluid such as water so that the entire apparatus is at a single temperature. This is not possible for the IR experiments conducted here since the IR beams must be brought into and out of the cell through a nonabsorbing medium. It was found that an oven containing the cell and all components connected to the cell provided the necessary uniformity of temperature. Five fans in the oven circulate the heated air. The oven was stringently tested. First, multiple thermocouples were placed at many points in the oven. Measurements taken over a wide range of temperatures showed excellent uniformity throughout the oven ( $< 0.3$  °C). Next, a thermocouple was inserted inside the sample chamber. The temperature measured by a platinum RTD attached to the outside of the cell matched the reading of the internal thermocouple within 0.1 °C, which is the resolution of the thermocouple readout. The final important test involved observing the disappearance of the liquid–gas meniscus at the critical point. This is not a simple test, as there is significant light scattering in the vicinity of the critical point, making the determination of the meniscus difficult at times. However, in both carbon dioxide and ethane, we were able to distinguish the critical temperature (i.e., the temperature at which the meniscus just disappears when the pressure  $\approx$  critical pressure) within 0.1 °C of the reported critical temperature, which is again the resolution of the temperature readout device. A hazy region, caused by light scattering from the existence of long-range density fluctuations, persists for a few tenths of a degree above the critical temperature. The HeNe laser beam shows no cylindrical distortion on passing through the cell. Therefore, the sample cell has uniform density, the temperature is controlled to  $\pm 0.1$  °C, and the pressure reading is accurate to within 0.8 psia (the limit of the 1500 psia transducer) for pressures  $< 1500$  psia and

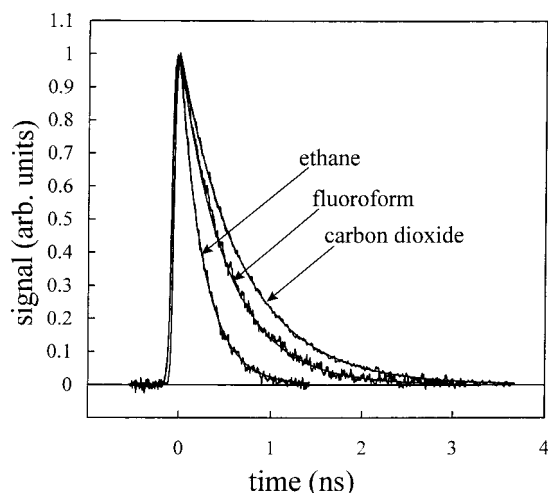


**Figure 1.** Pump-probe data for the asymmetric CO stretching mode of  $W(CO)_6$  in supercritical ethane (34 °C and 7.0 mol/L), fluoroform (28 °C and 7.5 mol/L), and carbon dioxide (33 °C and 10.6 mol/L). The data for each solvent are at approximately the same near-critical temperatures and densities relative to each fluid's critical point. Also shown in the figure are single-exponential fits giving the vibrational lifetimes ( $T_1$ ) of 267, 525, and 677 ps for ethane, fluoroform, and carbon dioxide, respectively. The data shows that the lifetime is significantly influenced by the solvent.

10 psia for pressures of >1500 psia (the limit of the 10 000 psia transducer).

All of the previously reported data were remeasured. It was found that only data within 2 K of the critical point and within a density range of approximately  $\rho_c - 25\%$  to  $\rho_c + 5\%$  were changed. All other previously reported data, including data taken as a function of temperature at fixed density,<sup>36</sup> are unchanged. However, in the course of retaking the data, improvements in the sample cell and in technique have reduced experimental scatter in the data.

In addition to lifetime measurements, infrared absorption measurements were made on all samples in the same cell using an FT-IR. The IR beam from the FT-IR was brought out of the instrument, passed through the sample cell, and then directed into a remote IR detector. The spectra were used to determine the wavelength for the  $T_1$  measurements at each density and temperature and to record the density and temperature dependence of the absorption line shifts, which are presented below.

### III. Experimental Results

Figure 1 shows sample pump-probe data for the asymmetric CO stretch of  $W(CO)_6$  in three different supercritical solvents: ethane (7.0 mol/L, 34 °C), carbon dioxide (10.6 mol/L, 33 °C), and fluoroform (7.5 mol/L, 28 °C). In all cases, the decays are fit well by single exponential functions. The data are all at approximately the critical density and 2° above the critical temperature for their respective solvents. The  $T_1$  values are 267, 525, and 677 ps in ethane, fluoroform, and carbon dioxide, respectively.  $T_1$  has a significant solvent dependence.

Figure 2 shows the lifetime data as a function of density in the three SCF solvents at ~2 K above the critical temperature  $T_c$  (upper panels) and at ~20 K above  $T_c$  (lower panels).  $T_c = 32.2, 25.9,$  and  $31.0$  °C for ethane, fluoroform, and  $CO_2$ , respectively. The near-critical isotherm temperatures for the three solvents were chosen so that the reduced temperatures are essentially the same. For the near-critical isotherm, the lifetime decreases rapidly as the density is increased from low density. As the critical density,  $\rho_c$ , is approached, the change

in the lifetime with density decreases. ( $\rho_c = 6.88, 7.54,$  and  $10.6$  mol/L for ethane, fluoroform, and  $CO_2$ , respectively.) The change in slope is more pronounced for  $CO_2$ . This is even more evident when the gas-phase (zero density) contribution to the lifetime is removed from the data (see below). In carbon dioxide, the lifetime decreases quite slowly at densities greater than ~7 mol/L. The lifetime decreases from 700 ps at 7 mol/L to about 600 ps at 20 mol/L, only a 15% drop over a three-fold increase in density. In contrast, in ethane, the lifetime changes from 263 ps at 7 mol/L to 176 ps at 13.3 mol/L, a 33% reduction in about a factor of two change in the density. The difference between the  $CO_2$  data and the other data will be discussed in section VI. The higher temperature isotherm data show a somewhat more uniform density dependence. Although the slope decreases with increasing density, there is a slightly smaller change in slope than in the near critical isotherm data.

A number of studies of electronic transitions<sup>10,11,20,21</sup> have displayed a three-regime density dependence. At low densities, the observables change rapidly with density. Over an intermediate density range around  $\rho_c$ , a plateau region exists where the observables are essentially density independent. At still higher densities, the observables once again change with increasing density. The previously published vibrational lifetime data<sup>8</sup> appeared to display a similar three-regime density dependence on the near-critical isotherm. However, the improved data, resulting from the very careful control of experimental conditions described in section II, do not display a distinct plateau region on the near critical isotherm. This will be discussed further in section VI.

In addition to measuring  $T_1$ , the CO asymmetric stretch absorption line position was measured as a function of density in the three solvents at the same two temperatures. Some of these data were reported previously,<sup>8</sup> and like the  $T_1$  data, the improved experimental apparatus produced small changes for data near the critical point. The new and improved results are presented in Figure 3 as the line position shift relative to the peak position at zero density. The absorption line position at zero density (gas-phase spectrum) is  $1997.3$   $cm^{-1}$ . The absorption line red shifts smoothly as the density is increased.

The lifetime measured as a function of density has two contributions, intramolecular and intermolecular. The intermolecular component of the lifetime arises from the influence of the fluctuating forces produced by the solvent on the CO stretching mode. This contribution is density dependent and is determined by the details of the solute-solvent interactions. The intramolecular relaxation is density independent and occurs at zero density through the interaction of the state initially prepared by the IR excitation pulse and the other internal modes of the molecule. To properly analyze the density dependence displayed in Figure 2, it is necessary to remove the contribution from intramolecular relaxation from the data. Figure 4 shows the extrapolation of six density-dependent curves (three solvents, each at two temperatures) to zero density. The spread in the extrapolations comes from making a linear extrapolation using only the lowest density data, which have the largest error bars. From the extrapolations, the zero density lifetime is ~1.1 ns.

To obtain a more accurate value of the intramolecular, zero density  $T_1$ , measurements were made on gas-phase  $W(CO)_6$  at zero solvent density.<sup>9</sup> A small amount of solid  $W(CO)_6$  was placed in an evacuated 1.5 cm long stainless steel cell with  $CaF_2$  windows. The pressure in the sample cell is the vapor pressure of  $W(CO)_6$ . The cell was heated to 326 K to increase the vapor pressure, producing an optical density of 0.5–1.0. FT-IR spectra of the sample displayed R, Q, and P rotational branches.



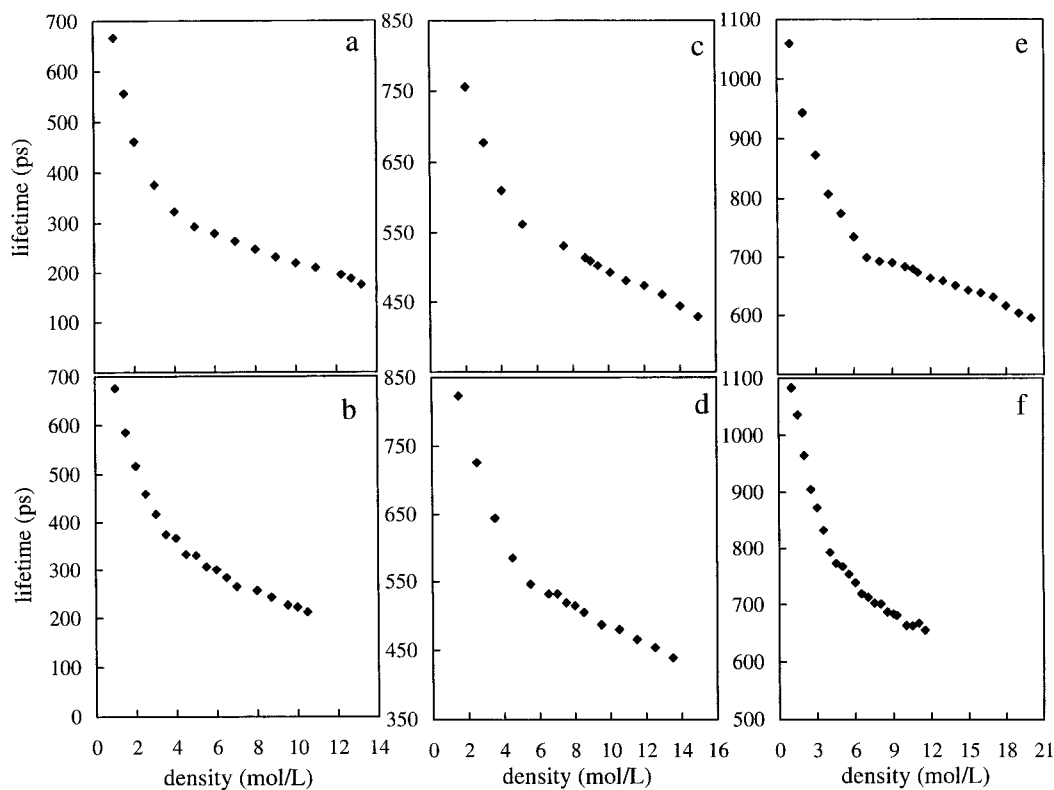


**Figure 2.** Vibrational lifetimes for the asymmetric CO stretching mode of  $W(CO)_6$  vs density along two isotherms of three supercritical fluids, ethane (34 °C panel a and 50 °C panel b), fluoroform (28 °C panel c and 44 °C panel d), and carbon dioxide (33 °C panel e and 50 °C panel f). The upper panel for each solvent is an isotherm at 2 °C above the critical temperature. In all six data sets, error bars (representing one standard deviation) are the size of the points or smaller.

Experiments discussed here were conducted on the Q branch. The infrared frequency was tuned so that it was at the peak of the Q branch at  $1997\text{ cm}^{-1}$ . The pressure is so low that the average collision time is many orders of magnitude longer than the time scale of the measurements.

As can be seen in Figure 1, the pump–probe decays are single exponentials. All pump–probe measured lifetime decays of the CO asymmetric stretch of  $W(CO)_6$  in SC solvents ethane,  $CO_2$  and fluoroform, over a wide range of densities ( $> 1\text{ mol/L}$ ) and temperatures, are single exponentials.<sup>7,8,36</sup> A single exponential (aside from orientational relaxation in liquids) is observed even when very fast pulses are used in the experiments.<sup>41</sup> Figure 5 displays data taken at 326 K on the gas-phase sample. The data are clearly nonexponential. The data can be fit very well with a triexponential. The average values obtained from a number of measurements are 140 ps, 1.28 ns, and  $> 100\text{ ns}$ . These values are substantially different, permitting reliable separation of the decay components. The slowest component is too slow to obtain an accurate value of the decay constant. The nature of this triexponential decay will be discussed in detail elsewhere.<sup>9</sup> Only the qualitative features will be described here.

From the extrapolation to zero density of the density-dependent  $1/T_1$  data in ethane, fluoroform, and  $CO_2$ , as well as from experiments in low-density Ar,<sup>9</sup> it is clear that  $T_1$  is the 1.28 ns decay component. This number is used below in the theoretical analysis of the density-dependent  $T_1$  experiments.

The long component in the decay is caused by “heating” of the low-frequency modes by the relaxation of the  $\sim 2000\text{ cm}^{-1}$  CO stretch. Since the relaxation occurs without collisions with the solvent, the energy remains in the molecule. Calculations using the known frequencies of all of the modes<sup>40</sup> show that depositing  $\sim 2000\text{ cm}^{-1}$  into the molecule raises the vibrational temperature from the initial 326 to 450 K. This produces a red

shift of the absorption spectrum, which was determined by temperature-dependent absorption measurements.<sup>9</sup> The pump–probe signal has two equal parts, ground-state depletion and stimulated emission. When the excited CO stretch relaxes into the density of low-frequency modes, the contribution to the signal from stimulated emission is lost. This reduces the signal 50%. However, since the spectrum shifts off of the probe pulse wavelength, recovery of the ground-state depletion at the probe wavelength does not occur. Therefore, the signal decays only 50%. In the absence of collisions that can cool the “heated” molecules, the signal will remain until cold molecules move into the probed volume. The signal will eventually recover as infrequent collisions cool the molecules and cold molecules from other parts of the cell move into the probe volume. We estimate that the time scale for these processes is approximately the same, i.e.,  $\sim 1\text{ }\mu\text{s}$ .

We propose that the fast component of the triexponential decay (140 ps) can be explained by the influence of the low-frequency modes of the molecule on the high-frequency CO stretch.<sup>9</sup> In the gas-phase vibrational experiment, prior to application of the pump pulse, the initial state of the molecule is prepared by its last collision with the wall of the cell or another molecule. The initial state is a complex superposition of eigenstates. Each mode,  $\lambda$ , will have some occupation number,  $n_\lambda$ . Under collision-free conditions, for a given molecule, the  $n_\lambda$  are fixed. At the 326 K sample temperature, the average total internal vibrational energy of a molecule is  $2900\text{ cm}^{-1}$  and the density of states at this energy (calculated with the harmonic approximation) is  $5 \times 10^5\text{ states/cm}^{-1}$ .<sup>48</sup> Thus, there are a vast number of initial states of the molecules that comprise the experimental ensemble. Absorbing a photon, which takes a molecule from the 0 to 1 state of the high-frequency CO stretch, changes the potential of the low-frequency

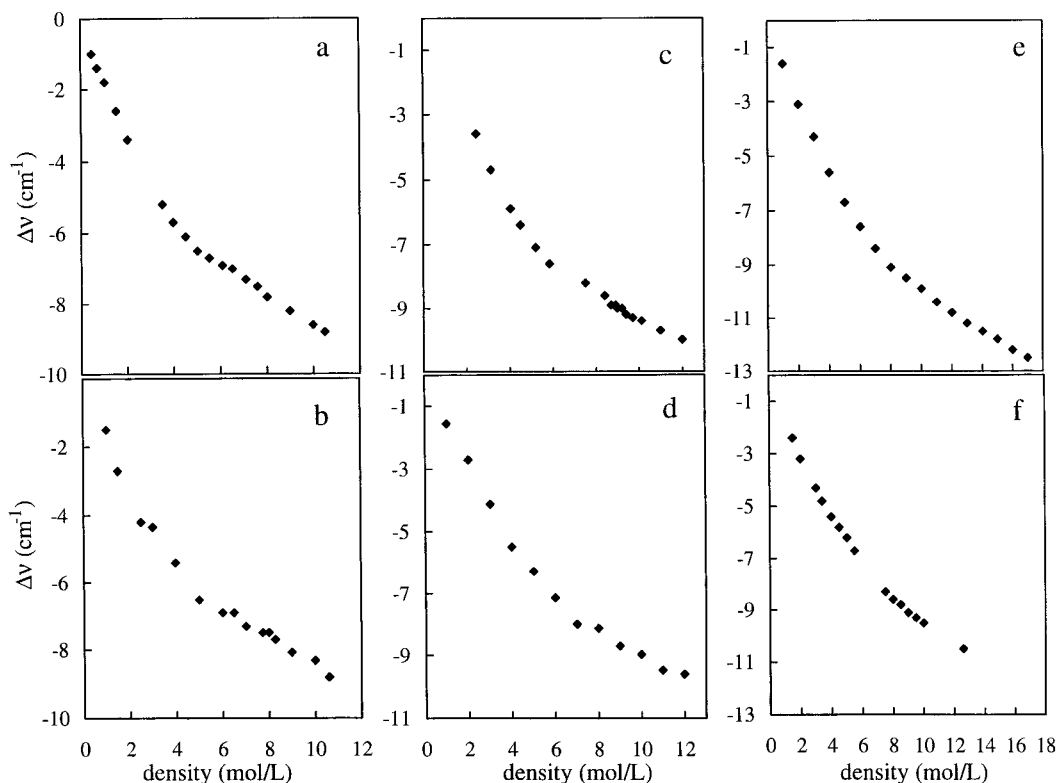


**Figure 3.** Vibrational line shift data for the asymmetric CO stretching mode of  $W(CO)_6$  vs density along two isotherms of three supercritical fluids, ethane (34 °C panel a and 50 °C panel b), fluoroform (28 °C panel c and 44 °C panel d), and carbon dioxide (33 °C panel e and 50 °C panel f). The data are presented as the difference between the absorption peak frequency and the gas phase (zero density) peak frequency in  $cm^{-1}$ . The negative sign means that the shift is to lower energy. The upper panel for each solvent is an isotherm at 2 °C above the critical temperature. Error bars in these curves are approximately  $0.1\ cm^{-1}$ .

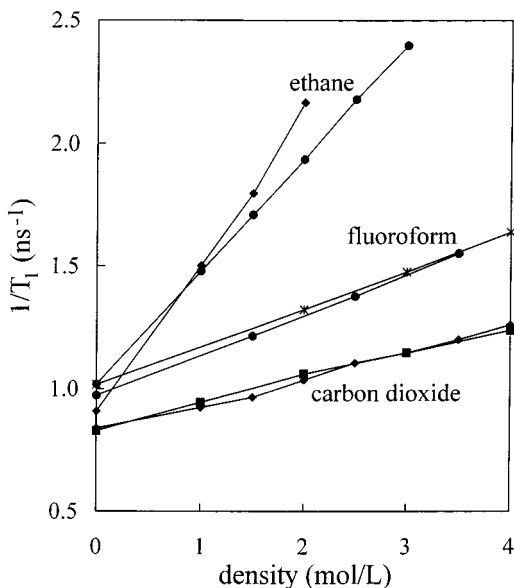


**Figure 4.** Vibrational relaxation rate data for the CO asymmetric stretch of  $W(CO)_6$  in various supercritical fluids at low densities. Extrapolation of the data to zero density gives an estimate of the gas-phase (collisionless) lifetime of  $\sim 1.1\ ns$ .

modes. The change in potential produces a time evolution that influences the CO stretch optical transition probability measured by the probe pulse. When a buffer gas or solvent is added, collisions cause the coherent evolution of the slow modes to be interrupted frequently, resulting in a narrowing of the CO asymmetric stretch 0–1 transition and possibly an averaging away of the perturbation responsible for the observed fast time

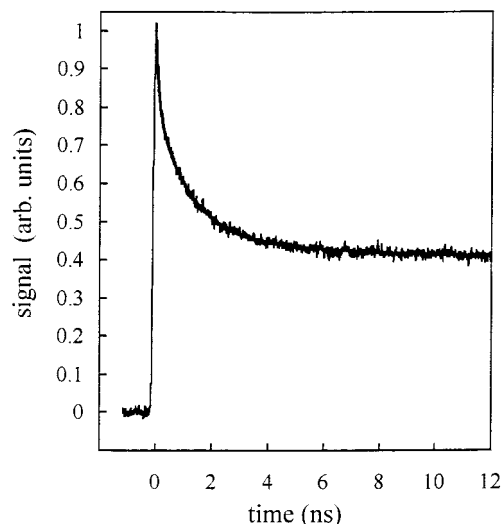


**Figure 5.** Typical pump–probe data for the CO asymmetric stretch of  $W(CO)_6$  in the gas phase at 326 K. The fit (barely discernible) is a triexponential with components 113 ps, 1.26 ns, and 157 ns. The values reported in the text are averages of many different data sets taken on many samples.

dependence. Thus, the fast component observed in these experiments<sup>9</sup> is inherently a low-pressure, gas-phase phenomenon.

Figure 6a shows a decay curve with a moderate pressure (0.05 mol/L) of Ar in the cell. The slow decay component is now noticeably faster, with a decay time of 8.1 ns. Collisions with Ar cool the low-frequency modes, allowing the spectrum to return to its initial wavelength, which results in ground-state recovery. Figure 6b shows data with an even higher Ar pressure

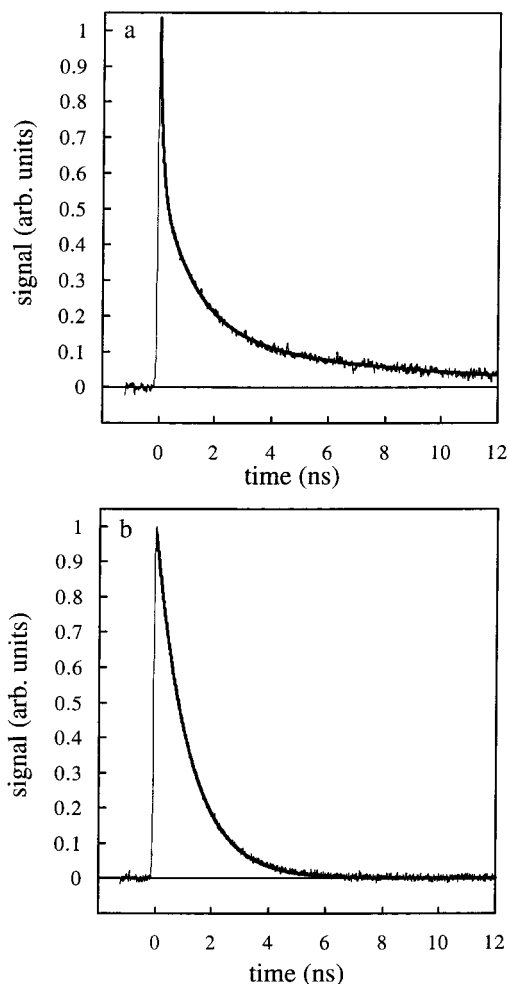


**Figure 6.** Sample pump-probe scans on the CO asymmetric stretch of  $\text{W}(\text{CO})_6$  in argon at two different pressures at 333 K (60 °C). (a) Pressure = 18 psia ( $\sim 1$  atm), argon density of  $\sim 0.05$  mol/L, and inverse collision frequency of  $\sim 0.2$  ns. The decay is fit with triexponential components 107 ps, 1.29 ns, and 8.1 ns. The long component has become substantially faster compared to collision free conditions. Argon promotes vibrational cooling of the excited  $\text{W}(\text{CO})_6$  molecules through collisions. The vibrational relaxation heating induced spectral shift, which is responsible for the long decay component, can decay on the experimental time scale. (b) Pressure = 1100 psia; argon density of  $\sim 3$  mol/L. The decay is now a single exponential with lifetime 1.20 ns. The fastest and slowest triexponential components observed in the gas phase (Figure 5) are eliminated by rapid collisions with argon at this high pressure (inverse collision frequency of  $\sim 3$  ps). The average lifetime obtained from several scans is unchanged from the gas-phase value, within experimental error.

(3.0 mol/L). The decay is now a single exponential. The collision induced cooling is fast compared to  $T_1$ , and the stimulated emission and ground-state depletion decay together, eliminating the long-lived component. It is interesting to note that the value of  $T_1$  remains unchanged although Ar is effective in causing the energy in the low-frequency modes to relax into the bath. The difference in the role played by Ar and the polyatomic SCF solvents will be discussed further below. Detailed analysis of the long component, including measurements on the P and R branches, will be presented in a subsequent publication.<sup>42</sup>

#### IV. Theory of $T_1$ Density Dependence

The theory starts with the standard relationship between the vibrational lifetime,  $T_1$ , and a classical description of the force-force correlation function,

$$k(\rho, T) = T_1^{-1} = \frac{Q}{2m\hbar\omega} \int_{-\infty}^{\infty} dt \langle F(t) F(0) \rangle_{\text{cl}} \cos(\omega t) \quad (1)$$

where  $m$  is the reduced mass of the oscillator and  $\omega$  is the Fourier transform frequency associated with energy deposition into the solvent.<sup>2</sup> For a diatomic,  $\omega$  is the oscillator frequency. However, for a polyatomic, an initially high-frequency mode can relax into lower frequency intramolecular modes, and  $\omega$  is the fraction of the initially excited oscillator energy that is deposited into the solvent.<sup>2</sup> This frequency is expected to be relatively low so that it falls within the solvent's spectral density.  $Q$  is called the quantum correction factor. As several authors have pointed out,<sup>43,44</sup> it is incorrect to directly replace the quantum mechanical correlation function with its classical analogue. The nature of the correction factor is a topic of considerable recent interest.<sup>44</sup> Several forms of  $Q$  have been suggested, and they are generally functions of temperature and the Fourier transform frequency. More discussion of the quantum correction factor will be given below.

As discussed in an earlier paper,<sup>1</sup> the force-force correlation function can be determined approximately using the methods of density functional theory. There it was shown that

$$T_1^{-1} \propto Q \int_0^{\infty} dt \cos(\omega t) \int d\mathbf{k} k^2 |\hat{C}_{21}(\mathbf{k})|^2 \hat{S}_1(\mathbf{k}, t) \quad (2)$$

where  $\hat{C}_{21}(\mathbf{k})$  is the Fourier transform of the direct correlation function between solute (component 2) and solvent (component 1), and  $\hat{S}_1(\mathbf{k}, t)$  is the dynamic structure factor of the solvent. The above expression for  $T_1$  is particularly useful for investigating vibrational relaxation in SCFs as it permits known density dependent thermodynamic solvent properties to be used in the calculation of the lifetime.

In the original implementation of eq 2, the  $k = 0$  limit of a hard sphere form of  $\hat{C}_{21}(\mathbf{k})$  was used along with the small  $k$  limit of  $\hat{S}_1(\mathbf{k}, t)$ . These approximations allowed eq 2 to be calculated analytically. However, the results were in only rough qualitative accord with the data. Furthermore, in the context of vibrational relaxation, small  $k$  approximations are not appropriate. To obtain a better description of vibrational relaxation in SCFs, we now evaluate eq 2 for all  $k$ . For this purpose, we take  $\hat{C}_{21}(\mathbf{k})$  as the direct correlation function of a binary hard sphere mixture, but now the full dependence on  $k$  is retained. Thus, we write  $\hat{C}_{21}(\mathbf{k})$  as<sup>45</sup>

$$\hat{C}_{21}(\mathbf{k}) = -2\pi(I_1 + I_2) \quad (3)$$

The variables  $I_1$  and  $I_2$  depend not only on  $k$  but also on  $R_1$  and  $R_2$  (the solvent and solute hard sphere diameters, respectively) and  $\rho_1$  and  $\rho_2$  (the solvent and solute number densities, respectively). The complete expressions for  $I_1$  and  $I_2$  are provided in Appendix A.

To motivate the form of the dynamic structure factor that is used in the theory, first consider its small  $k$  limit. For small  $k$ ,  $\hat{S}_1(\mathbf{k}, t)$  can be determined from hydrodynamics as the solution to the coupled equations for the conservation of mass, momentum, and energy, which leads to<sup>46</sup>

$$\hat{S}_1(\mathbf{k}, t) = \hat{S}_1(\mathbf{k}) \left[ \left(1 - \frac{1}{\gamma}\right) e^{-D_T k^2 t} + \frac{1}{\gamma} \cos(c_s k t) e^{-\Gamma k^2 t} \right] \quad (4)$$

Here  $\hat{S}_1(\mathbf{k})$  is the equilibrium structure factor of the solvent, which we approximate by the Ornstein-Zernike expression, given by<sup>46</sup>

$$\hat{S}_1(\mathbf{k}) = \frac{\rho_1 \kappa_T / \kappa_T^0}{1 + k^2 \xi^2} \quad (5)$$

where  $\rho_1$  is the number density of the solvent,  $\kappa_T$  is its isothermal compressibility,  $\kappa_T^0$  is the isothermal compressibility of the ideal gas, and  $\xi$  is the correlation length of the density fluctuations. Further,  $\gamma \equiv C_p/C_V$  is the ratio of constant pressure and volume specific heats,  $D_T$  is the thermal diffusivity,  $c_s$  is the adiabatic speed of sound, and  $\Gamma$  is the sound attenuation constant. In theoretical analysis of light scattering experiments, the first term in eq 4 gives rise to the zero-frequency Rayleigh peak that is associated with thermal diffusion, while the second term corresponds to twin Brillouin peaks at frequencies  $\pm c_s k$  from the Rayleigh peak that are associated with sound propagation.

Numerical analysis of  $\hat{S}_1(\mathbf{k}, t)$  shows that contributions to the  $k$  integral in eq 2 are overwhelmingly dominated by the function at large  $k$ , i.e.,  $k \approx 1 \text{ \AA}^{-1}$ . In eq 4, the  $k$ -dependent decay constant,  $1/\tau_1(k)$ , ( $D_T k^2$  in eq 4) can be extended to essentially all  $k$  using the following approximation developed by Kawasaki<sup>47</sup>

$$\frac{1}{\tau_1(k)} = \frac{k_B T}{8\pi\eta\xi^3} \left[ 1 + k^2 \xi^2 + \left( k^3 \xi^3 - \frac{1}{k\xi} \right) \tan^{-1}(k\xi) \right] \quad (6)$$

where  $\eta$  is the viscosity. In the limit  $k\xi \ll 1$ , eq 6 reduces to  $D_T k^2$ .

Since we need to evaluate eq 2 at very large  $k$  only, we have determined that  $1/\tau_2(k)$  ( $\Gamma k^2$  in eq 4) becomes sufficiently large that the second term in brackets in eq 4 can be neglected in comparison to the first. Neglecting  $1/\tau_2(k)$  at large  $k$  is supported by both experiment and theory. For small  $k$ , acoustic waves can propagate in the fluid as in a continuum, because the wavelength is much longer than the average intermolecular spacing. In a crystal, the shortest wavelength for a propagating wave is twice the lattice spacing. In a fluid, as the wavelength approaches the average solvent intermolecular spacing, a propagating wave will experience the disorder of the fluid, and such a wave will damp rapidly. For even shorter wavelengths, wave propagation is not possible. These qualitative ideas are born out by neutron scattering experiments<sup>48–51</sup> and molecular dynamics simulations.<sup>52–54</sup> Neutron scattering experiments show that either the Brillouin lines are absent or extremely broad at large  $k$ . The broad line width is attributed to very rapid damping of large  $k$  acoustic waves, i.e.,  $\Gamma$  becomes very large. Hard-sphere molecular dynamics simulations also show that  $\Gamma$  becomes large at large  $k$  and that at sufficiently large  $k$  ( $k \approx 1.5/\text{solvent diameter } \text{\AA}^{-1}$ ), acoustic waves do not exist.<sup>52</sup> These considerations demonstrate that the propagating wave term in eq 4 becomes negligible for sufficiently large wavevectors.

Therefore, for large  $k$  the dynamic structure factor is given by

$$\hat{S}_1(\mathbf{k}, t) = \hat{S}_1(\mathbf{k}) \left[ \left( 1 - \frac{1}{\gamma} \right) e^{-t/\tau_1(k)} \right] \quad (7)$$

with  $1/\tau_1$  given by the Kawasaki expression, eq 6. As stated, careful numerical inspection of the  $k$  integral in eq 2 shows that all of the contribution to the integral occurs for  $k$  sufficiently large that eq 7 is the appropriate form of the dynamic structure factor for evaluation of the integral. Equation 4 is never used in the calculations, but it was presented to motivate the form of eq 7.

As mentioned above,  $Q$  in eq 2 is a quantum correction factor. A number of quantum corrections have been suggested depending on the nature of the system. Most involve a function of the temperature and the oscillator frequency and apply to simple model theoretical systems. One form that seems to be more generally applicable is due to Egelstaff.<sup>55</sup> Egorov and Skinner recently tested several correction factors on exactly solvable systems, as well as vibrational relaxation in liquid oxygen.<sup>44</sup> The Egelstaff correction performed the best overall. The Egelstaff correction is given by a prefactor

$$Q = e^{\hbar\omega/2kT} \quad (8a)$$

and the time variable,  $t$ , is replaced as

$$t \rightarrow \sqrt{t^2 + (\hbar/2k_B T)^2} \quad (8b)$$

in the classical force–force correlation function. In eq 2, only the dynamic structure factor component of the force–force correlation function,  $\hat{S}_1(\mathbf{k}, t)$ , contains  $t$ , and the substitution, (8b), is made in this term. Equation 2 is evaluated using eqs 3, 7, and 8. The time integral in eq 2, including the Egelstaff correction factor, can be performed analytically. The  $k$  integral is performed numerically.

Before preceding, it is useful to consider the form of the force–force correlation function which is given in eq 2 with eqs 3, 7, and 8. The form of the force–force correlation function, derived using density functional formalism, is employed because it permits the use of very accurate equations of state and other experimentally determined properties for solvents such as ethane and CO<sub>2</sub> to describe the density dependence and temperature dependence of the solvent properties. These equations of state hold near the critical point as well as away from it. Using the formalism presented above, we are able to build the known density and temperature-dependent properties of the solvent into the theory of vibrational relaxation. There is a choice inherent in the approach we have employed. We build in a very accurate description of the solvent properties and how they change with density and temperature. This is not doable using other approaches for the development of the force–force correlation function.<sup>56</sup> In exchange for the detailed description of the solvent, we have made more approximate the description of the force–force correlation function. All theories of vibrational relaxation are approximate. The real question is what is necessary to provide a good description of the system under study.

A proper force–force correlation function is Gaussian at short time (the inertial dynamics of the solvent).<sup>56</sup> The Gaussian behavior is usually modeled as  $1 - at^2$ , where  $a$  is a constant. Following this initial rapid drop, the decay becomes slower, reflecting structural dynamics of the solvent. The longer time behavior can have a complicated functional form. If the Fourier transform in eq 2 is taken at very high frequency, the very short time inertial component of the correlation function will make the major contribution. Thus, to calculate the vibrational relaxation of a high-frequency diatomic, properly describing the inertial part of the correlation function is essential. However, for a polyatomic molecule, in which most of the energy flows into a combination of intramolecular modes, the Fourier transform frequency,  $\omega$ , will be a substantially lower frequency than the initially excited oscillator frequency, and the details of the very short time behavior of the correlation function will be less important.

The force–force correlation function used here has a complicated form that can be determined by numerical evaluation.



We examined the correlation function for ethane at 50 °C and the critical density. With the Egelstaff quantum correction, the correlation function initially decays as  $1 - at^2$  for a very short time ( $\sim 15$  fs). It then slows and becomes progressively slower at longer times. As mentioned above and will be discussed in detail in connection with the experiments, the Fourier transform is taken at a relatively low frequency ( $150\text{ cm}^{-1}$ ), not the  $2000\text{ cm}^{-1}$  oscillator frequency. For low frequencies, the very short time details of the correlation function are not of prime importance. Without the quantum correction, the strictly classical correlation function does not begin with zero slope at zero time, but rather, it initially falls steeply. However, the quantum corrected function and the classical function have virtually identical shapes after  $\sim 15$  fs. As will be demonstrated below, the force-force correlation function contained in eq 2 with eqs 3, 7, and 8 does a remarkable job of reproducing the density dependence observed experimentally, which is of interest here. It will be shown in a subsequent publication that the treatment given here also works very well for describing the temperature dependence of the vibrational relaxation at a number of fixed densities. While the correlation function does not rigorously have the correct short time functional form, by incorporating a detailed description of the solvent properties, it is able to provide a very good description of the vibrational relaxation as a function of density and temperature.

A wide variety of density- and temperature-dependent input parameters are required to evaluate eq 2. These include  $\rho_1$ , the number density of the solvent,  $\kappa_T$ , the isothermal compressibility,  $\xi$ , the correlation length of density fluctuations,  $\gamma \equiv C_p/C_v$ , the ratio of specific heats, and  $\eta$ , the viscosity. Very accurate equations of state for ethane<sup>57–59</sup> and  $\text{CO}_2$ <sup>59</sup> are available that provide the input information. The necessary input parameters for fluoroform were obtained by combining information from a variety of sources.<sup>60–62</sup> There is somewhat greater uncertainty in the fluoroform parameters.

The thermodynamic and hydrodynamic parameters that enter the theory build in a detailed description of the SCF solvent. All of these input parameters vary substantially with density and temperature. In the near-critical region, the variations of the parameters are very large. In comparing the theory with experiment in the next section, the thermodynamic parameters of the solvent feed into the calculations. As discussed below, the zero density  $T_1$  is removed from the data shown in Figure 2, and the resulting density and temperature-dependent lifetimes,  $T_1(\rho, T)$ , are compared to the theory. The theoretical curves are scaled to match the data at one point. The solute and solvent hard sphere diameters are also required as input into the calculations. The results are not highly sensitive to the solute diameter, but they are sensitive to the solvent diameter.

The adjustable parameter in eq 2 that has a substantial effect on the shape of the curves is the frequency,  $\omega$ . In a diatomic,  $\omega$  is the frequency of the vibrational transition since all of the energy must be deposited into the solvent for relaxation to occur. For a high-frequency mode of a polyatomic with many lower frequency modes, a substantial amount of energy can go into internal modes of the molecule.<sup>63</sup> This is clear from the data in Figure 5, which shows that vibrational relaxation of the  $\sim 2000\text{ cm}^{-1}$  CO asymmetric stretch can occur even in the absence of solvent. For a polyatomic,  $\hbar\omega$  corresponds to the energy that is deposited into the solvent when vibrational relaxation occurs. The solvent can open up relaxation pathways that are not available to the isolated molecule by providing a means to conserve energy.  $\omega$  would be expected to fall within the solvent's spectral density. Since the details of the pathway or

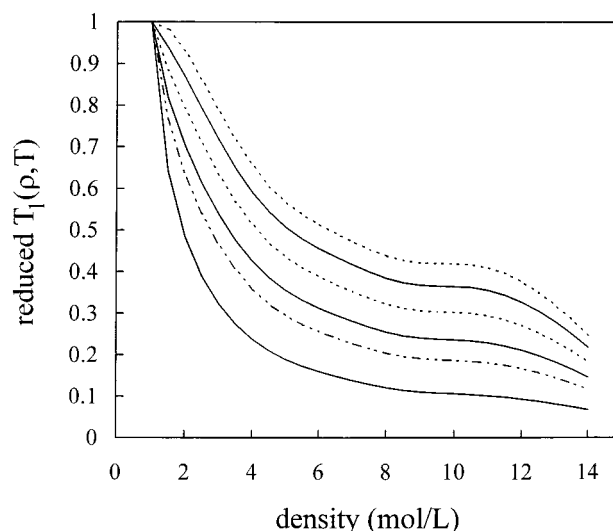


**Figure 7.** Calculations of  $T_1(\rho, T)$  vs  $\rho$  for several  $\omega$ . The input parameters are those for the solvent ethane at 34 °C. The calculations are shown as reduced lifetimes, i.e., each curve is normalized at 1 mol/L. The curves, from top to bottom, correspond to  $\omega$  values 2000, 1000, 500, 250, 150, and  $50\text{ cm}^{-1}$ .

pathways for relaxation are not known, the frequency  $\omega$  is used as an adjustable parameter to fit the data. Figure 7 shows calculations of  $T_1(\rho, T)$  vs  $\rho$  for several  $\omega$ . The input parameters are those for the solvent ethane at 34 °C (see below for more details). The calculations are shown as reduced lifetimes, i.e., each curve is normalized at 1 mol/L. The Fourier transform frequency for each curve is given in the figure caption. The results show that both the shape of the curves and the magnitude of the density dependence change with  $\omega$ . As the frequency is increased, the lifetime changes less with increasing density. The highest frequency curves may have substantial error because they will depend on the details of the very short time portion of the force-force correlation function.

## V. Comparison of Theory and Experiment

Equation 2 describes the contribution to the vibrational lifetime arising from interactions of the solute with the solvent. Comparisons between theory and data are made by removing the contribution from the zero density, gas-phase lifetime,  $T_1^g = 1.28 \pm 0.1\text{ ns}$ , from  $T_1^m$ , the measured density-dependent lifetimes, to give  $T_1(\rho, T)$ , i.e.,

$$\frac{1}{T_1(\rho, T)} = \frac{1}{T_1^m} - \frac{1}{T_1^g} \quad (9)$$

Figure 8a shows  $T_1(\rho, T)$  vs density for the solvent ethane at 34 °C and the best fit theoretically calculated curve. The theory was scaled to match the data at the critical density, 6.88 mol/L. The best agreement was found for  $\omega = 150\text{ cm}^{-1}$ . The solute hard sphere diameter, 6.70 Å, was determined from the crystal structure.<sup>64</sup> The solvent hard sphere diameter, 3.94 Å, is an  $\sim 7\%$  reduction from the literature value.<sup>65</sup> It is seen that the theory does a very creditable job of reproducing the density dependence of the data. Figure 8b shows the 50 °C data for the ethane solvent and the theoretically calculated curve. In this calculation, *there are no adjustable parameters*. The scaling factor, frequency  $\omega$ , and the hard sphere diameters are the same as those used in the fit of the 34 °C data. The agreement is quite remarkable.

The  $T_1(\rho, T)$  data in ethane show only a small change in going from 34 to 50 °C. The theory is able to reproduce the data at



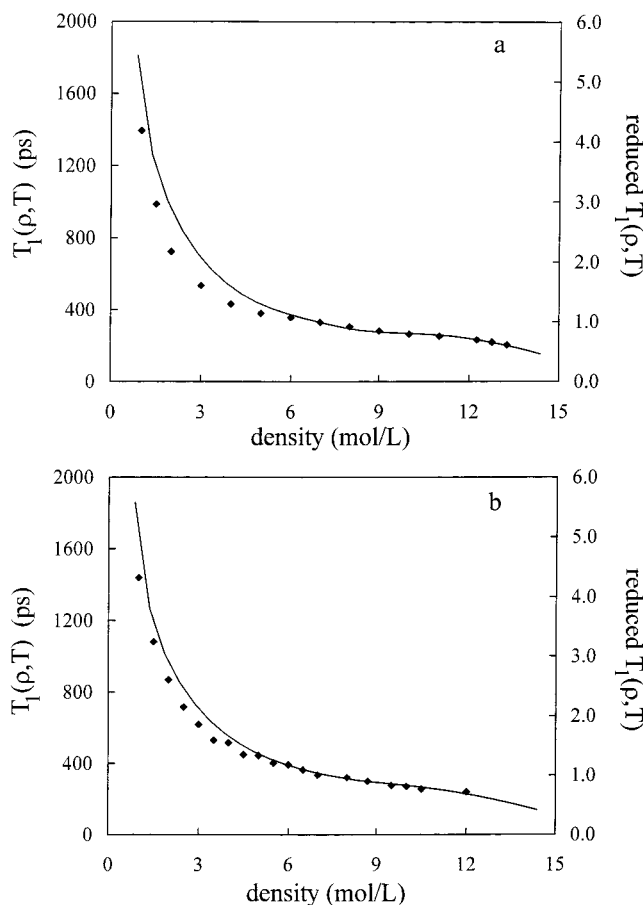


**Figure 8.** (a)  $T_1(\rho, T)$  vs density for the solvent ethane at 34 °C and the best fit theoretically calculated curve. The theory was scaled to match the data at the critical density, 6.88 mol/L. The best agreement was found for  $\omega = 150 \text{ cm}^{-1}$ . Agreement between theory and data is good. (b)  $T_1(\rho, T)$  vs density for the solvent ethane at 50 °C and the best fit theoretically calculated curve. The curve is calculated with *no adjustable parameters*. The scaling factor, frequency  $\omega$ , and the hard sphere diameters are the same as those used in the fit of the 34 °C data. The agreement between theory and experiment is very good.

both temperatures even though the system undergoes substantial changes in going from one temperature to another. Figure 9 shows plots of the solvent parameters that enter the theory vs density at the two temperatures. As can be seen, most of the curves change substantially with temperature. However, these changes balance out in the theory to give curves that are in accord with the small changes in the data. Omission of any of these temperature-dependent factors makes the theoretical agreement poor.

Figure 10 shows  $T_1(\rho, T)$  measured in fluoroform. Figure 10a is data on the near critical isotherm, i.e., 2 K above  $T_c$ . The calculated curve is scaled to match the data at the critical density, 7.54 mol/L.  $\omega$  is not adjustable, but set equal to  $150 \text{ cm}^{-1}$ , the value obtained in the fit of the data taken in ethane. An accurate value of the effective hard sphere diameter is not available for fluoroform.<sup>65</sup> Effective hard sphere diameters are temperature dependent, becoming smaller as the temperature is increased.<sup>65</sup> X-ray data is available at 70 K, well below the experimental temperature.<sup>66</sup> The 70 K X-ray data yields a hard sphere diameter of 4.60 Å. The best agreement with the  $T_1(\rho, T)$  at 28 °C is obtained with 3.28 Å. While this is a significant reduction from the 70 K X-ray determined value, it is not known how it would compare to a good value of the effective hard sphere diameter at 28 °C (301 K). The theory does a good job of reproducing the density dependence of the data by only adjusting

the solvent size as a fitting parameter that affects the shape. Figure 10b shows data taken at 44 °C, which is the equivalent increase in temperature above  $T_c$  as the higher temperature data taken in ethane (Figure 8b). The calculated curve is obtained using the thermodynamic input parameters for the higher temperature and the scaling factor from 28 °C.  $\omega = 150 \text{ cm}^{-1}$  and the fluoroform diameter is 3.28 Å. As with the data taken in ethane, the theory does a good job of reproducing the higher temperature data *with no adjustable parameters*.

As shown in Figure 7, the calculations are sensitive to the choice of  $\omega$ . The fact that the same  $\omega$  gives good agreement between the  $T_1(\rho, T)$  data in both ethane and fluoroform suggests that this is not an arbitrary value, but rather may reflect the actual energy deposited in the solvent in the course of the vibrational relaxation. A number of calculations were performed to examine the influence of  $\omega$  on the calculated values of  $T_1(\rho, T)$ . The curves in Figure 7 are all for single values of  $\omega$ . Calculations were also performed in which a distribution of  $\omega$  was used. It was found that  $\omega$  need not be a single frequency in order to produce curves with the same shapes as those shown in Figure 7. For instance, relaxation times calculated by averaging over a Gaussian distribution of frequencies with a mean of  $150 \text{ cm}^{-1}$  and a standard deviation of  $20 \text{ cm}^{-1}$  gave results identical to the results of a calculation using a single fixed frequency of  $150 \text{ cm}^{-1}$ . This frequency is most likely located in the single “phonon” density of states (DOS) of the continuum of low-frequency modes of the solvents. Instantaneous normal mode calculations in  $\text{CCl}_4$ ,  $\text{CHCl}_3$ , and  $\text{CS}_2$  show cutoffs in the DOS at  $\sim 150$ ,  $\sim 180$ , and  $\sim 200 \text{ cm}^{-1}$ , respectively.<sup>67,68</sup> The higher frequency portions of the DOS are dominated by orientational modes. Since ethane, fluoroform, and  $\text{CO}_2$  are much lighter than the liquids cited above, it is expected that their DOS will extend to substantially higher frequency.

In the gas phase, the asymmetric CO stretch lifetime is 1.28 ns. The role of the solvent may be to provide an alternative relaxation pathway that requires single phonon excitation (or phonon annihilation)<sup>63</sup> around  $150 \text{ cm}^{-1}$ . Some support for this picture is provided by the results shown in Figure 6. When Ar is the solvent at 3 mol/L, a single-exponential decay is observed with a lifetime that is the same as the zero density lifetime, within experimental error. While Ar is effective at relaxing the low-frequency modes of  $\text{W}(\text{CO})_6$ , as discussed in conjunction with Figure 6, it has no effect on the asymmetric CO stretch lifetime. The DOS of Ar cuts off at  $\sim 60 \text{ cm}^{-1}$ .<sup>69</sup> If the role of the solvent is to open a relaxation pathway involving intermolecular interactions that require the deposition of  $150 \text{ cm}^{-1}$  into the solvent, then in Ar, the process would require the excitation of three phonons. A three-phonon process would be much less probable than single-phonon processes that could occur in the polyatomic solvents. In this picture, the differences in the actual lifetimes measured in ethane, fluoroform, and  $\text{CO}_2$  (see Figure 2) are attributed to differences in the phonon DOS around  $150 \text{ cm}^{-1}$  or to the magnitude of the coupling matrix elements.

Figure 11 shows a comparison of  $T_1(\rho, T)$  data with calculated curves for the  $\text{CO}_2$  solvent at two temperatures, 33 °C (2 K above  $T_c$ ) and 50 °C. The calculated curves are scaled to the data at 33 °C and 2 mol/L. Again,  $\omega = 150 \text{ cm}^{-1}$ . The solvent hard sphere diameter is 3.60 Å.<sup>65</sup> The agreement between theory and experiment, while good at low density, is clearly not as good as that displayed for ethane (Figure 8) and fluoroform (Figure 10) at higher densities. Adjusting  $\omega$  does not improve the agreement between theory and data nor does a variation of the solvent diameter. The  $T_1(\rho, T)$  data appears to differ from

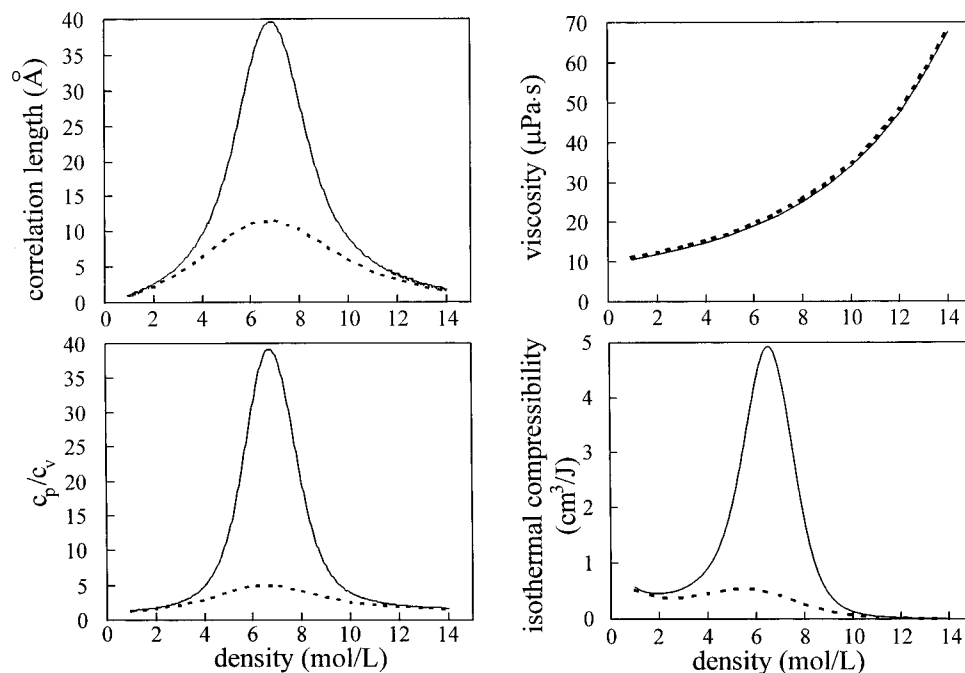


**Figure 9.** Plots of the ethane solvent parameters vs density for the parameters that enter the theory at the two temperatures, 34 °C (solid lines) and 50 °C (dashed lines) that correspond to the data and theory curves in Figure 8.

the data in the other two solvents. After the initial rapid decrease in the lifetime as the density is increased from 1 mol/L, the data curve with CO<sub>2</sub> as the solvent is much flatter than the data obtained with the other two solvents.

## VI. Discussion

The theory does a very good job of reproducing the density-dependent solvent contribution to the vibrational lifetimes,  $T_1(\rho, T)$ , at two temperatures in the supercritical solvents ethane and fluoroform. The theory does less well when CO<sub>2</sub> is the solvent. The theory uses a variety of solvent properties that captures the details of the changes in the solvent with density. The spatial distribution of the solvent about the solute enters through the hard sphere direct correlation function, which contains no attractive components. Thus, the theory contains no specific solute–solvent “clustering” per se. In the ethane and fluoroform solvents, the theory is able to reproduce the data near the critical point with reasonable accuracy. The presence of the critical point comes into the theoretical calculations through the behavior of the solvent input parameters. The substantial changes in the parameters near the critical point are illustrated in Figure 9. Thus, any role that critical phenomena may play in the vibrational relaxation enter through the solvent properties alone, not through augmentation of near critical local density fluctuations caused by attractive solute–solvent interactions.

An interesting question arises as to why the theory does not do as good a job of reproducing the data with CO<sub>2</sub> as the solvent. As mentioned above, the data with CO<sub>2</sub> as the solvent becomes much flatter above ~6 mol/L than the data taken in the other two solvents. The theoretical curves with the CO<sub>2</sub> solvent have shapes that are similar to the theoretical and data curves for the other two solvents. This might suggest that the CO<sub>2</sub> solvent data is modified by some special chemical interaction. The source of the discrepancy between theory and data does not appear to be associated with near critical phenomenon since the discrepancy for the near critical isotherm is not reduced for the higher temperature isotherm. One might speculate that there

is a specific interaction between CO<sub>2</sub> and W(CO)<sub>6</sub>. Supercritical CO<sub>2</sub> tends to form T-shaped structures with the oxygen of one CO<sub>2</sub> coordinated with the carbon of another CO<sub>2</sub>, forming a T.<sup>70</sup> It is possible that CO<sub>2</sub> has a tendency to coordinate with the oxygens of W(CO)<sub>6</sub> in the same manner. Such a specific interaction could modify the density dependence of the vibrational lifetime. While such a specific interaction is an appealing explanation given the very good agreement between theory and experiment in ethane and fluoroform, the reduced quality of the agreement for the CO<sub>2</sub> data may simply reflect inadequacies in the theory.

While the  $T_1(\rho, T)$  data taken in CO<sub>2</sub> solvent becomes quite flat at higher densities, the same is not true of the vibrational line shift data (Figure 3). The line shift with increasing density in CO<sub>2</sub> at the two temperatures becomes only slightly more mild at high density. In all three solvents, the  $T_1(\rho, T)$  density dependence has a greater change in slope with density than the line shift data.

There is no counterpart of the  $T_1(\rho, T)$  theory for the calculation of the vibrational line shifts. Egorov and Skinner have recently developed a theory for the line shift as a function of density and temperature.<sup>71</sup> The theory uses a Lennard–Jones potential with spherical solute and solvent molecules to describe solute–solvent interactions. Egorov and Skinner can reproduce some of the line shift<sup>71</sup> and  $T_1$ <sup>72</sup> data presented here using their theory. To do so requires a significant attraction between the solute and solvent, a feature that is not contained in the  $T_1(\rho, T)$  theory presented here. The  $T_1$  theory presented here contains much more detailed information on the density and temperature-dependent properties of the solvent than the Egorov–Skinner theory, but the Egorov–Skinner theory uses a form of the solute/solvent interaction which enables them, through adjustable parameters, to control the solute/solvent spatial distribution.

The vibrational line shift data in carbon dioxide look quite similar to the experimental results of Blitz et al.<sup>73</sup> and Pan et al.<sup>74</sup> Blitz and co-workers examined the density dependence of the  $3\nu_3$  absorption line ( $\sim 6950$  cm<sup>-1</sup>) of pure supercritical CO<sub>2</sub> at 50 °C.<sup>73</sup> The MacPhail group<sup>74</sup> measured Raman spectra of

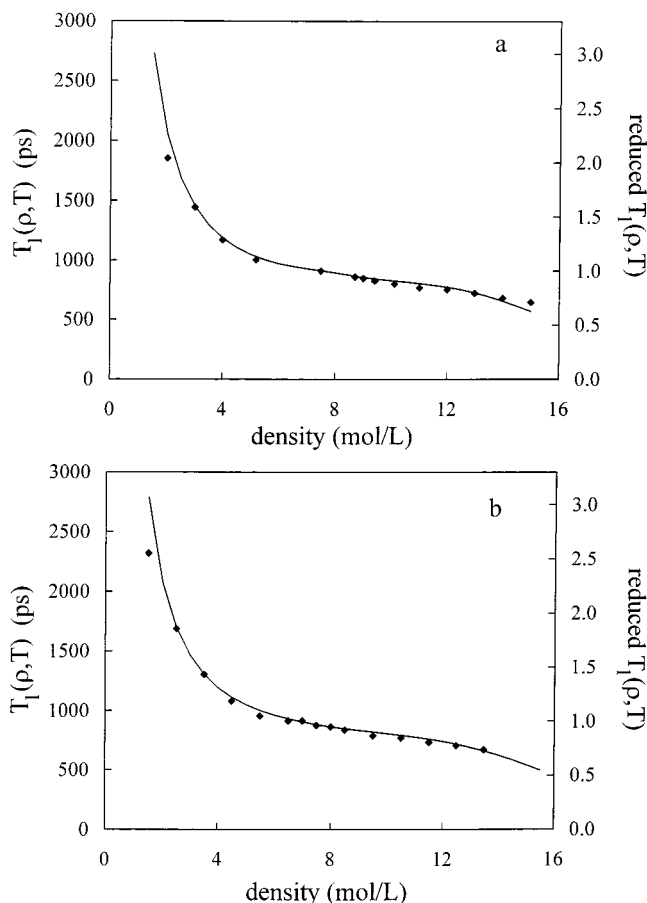


**Figure 10.** (a)  $T_1(\rho, T)$  data measured in fluoroform on the near critical isotherm (28 °C), 2 K above  $T_c$ , and the calculated curve, which is scaled to match the data at the critical density, 7.54 mol/L.  $\omega$  is not adjustable, but set equal to 150  $\text{cm}^{-1}$ , the value obtained in the fit of the data taken in ethane. The theory does a good job of reproducing the shape of the data. (b)  $T_1(\rho, T)$  data taken at 44 °C, which is the equivalent increase in temperature above  $T_c$  as the higher temperature data taken in ethane (Figure 8b). The calculated curve is obtained by using the thermodynamic input parameters for the higher temperature and no adjustable parameters. The theory does a good job of reproducing the higher temperature data.

the C–H stretch of cyclohexane- $d_{11}$  in supercritical  $\text{CO}_2$ , also at 50 °C. They observed that the C–H stretch (both axial and equatorial) Raman peaks shift very mildly with density. The  $3\nu_3$  shift is somewhat more than the shift observed for the CO asymmetric stretch of  $\text{W}(\text{CO})_6$  in  $\text{CO}_2$ , and the C–H stretch shift is somewhat less. No obvious manifestation of critical phenomena is observed in these data, but at 50 °C, which is substantially above  $T_c$  for  $\text{CO}_2$ , it is not clear that any would be observed even if critical phenomena were important on a near critical isotherm. The spectral data for the asymmetric CO stretch of  $\text{W}(\text{CO})_6$  in  $\text{CO}_2$  on the 50 °C and 33 °C (near critical) isotherms are so similar (as are the  $T_1(\rho, T)$  data on the same isotherms) that they do not suggest any special attributes of critical phenomena are important. The critical properties of the solvent are important insofar as they influence the density dependence of the solvent parameters (see Figure 9).

The observations in these vibrational experiments are different from observations made on electronic excited states. Vibrational cooling following electronic excitation<sup>10</sup> and solvatochromic shifts involving electronic transitions<sup>11,20,21</sup> do appear to be different on a near critical isotherm than at higher temperatures. It is possible that solvent reorganization, which occurs upon electronic excitation, may play a role in the apparent sensitivity

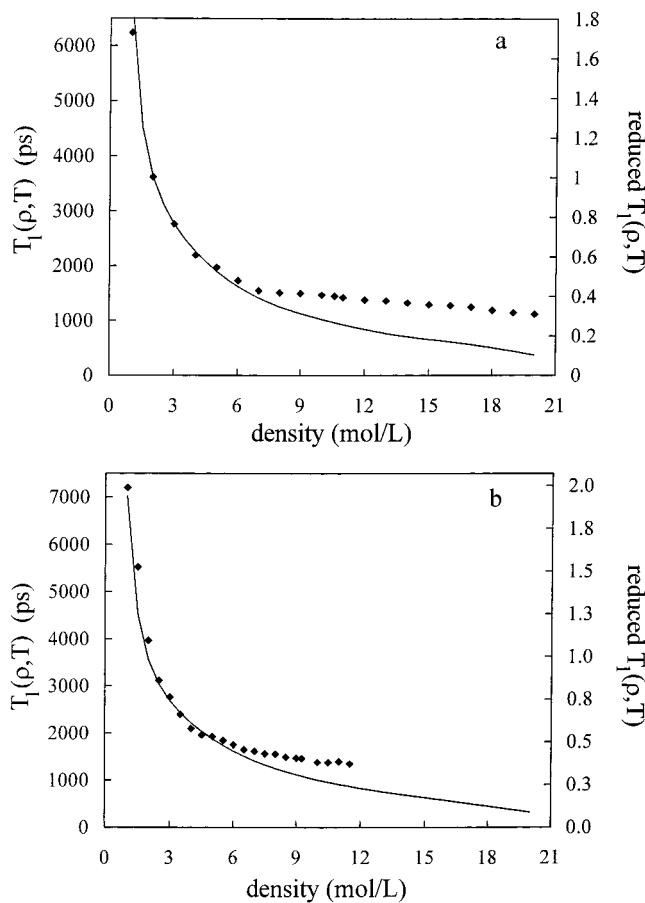


**Figure 11.**  $T_1(\rho, T)$  data with calculated curves for the  $\text{CO}_2$  solvent at two temperatures, 33 °C (2 K above  $T_c$ ) and 50 °C. The calculated curves are scaled to the data at 2 mol/L and 33 °C.  $\omega = 150 \text{ cm}^{-1}$  and the solvent hard sphere diameter is 3.60 Å. The agreement between theory and experiment, while good at low density, is clearly not as good as that displayed for ethane (Figure 8) and fluoroform (Figure 10) at the higher densities.

of the electronic excited state observables to proximity to the critical point.

The vibrational lifetime and vibrational line shift data taken as a function of density in three solvents show little change in form upon going from near critical isotherms to higher temperature isotherms. The  $T_1$  theory presented here, which uses detailed inputs of the solvent properties but treats the solute/solvent spatial distribution in terms of hard spheres, is able to reproduce the data with considerable accuracy. The theory takes into account near-critical behavior through the density dependence of the solvent properties. For the systems studied, the combination of experiment and theory indicate that there is no need to invoke critical density enhancement or solvent clustering about the solute to describe the data.

**Acknowledgment.** We thank Professor J. L. Skinner, Department of Chemistry, University of Wisconsin at Madison, for many informative conversations pertaining to vibrational relaxation. We also thank the Air Force Office of Scientific research which made this work possible through Grant F49620-94-1-0141. D.J.M. acknowledges the NSF for a graduate fellowship. M.S. thanks the Mitsubishi Chemical Corporation for supporting his participation in this research.

## Appendix A

The following equations are used in the calculation of the direct correlation function, eq 3:<sup>45</sup>

$$I_1 = \frac{2a_1}{k} \left[ -\frac{\lambda}{k} \cos(k\lambda) + \frac{1}{k^2} \sin(k\lambda) \right] \quad (\text{A1})$$

$$I_2 = a_1 I_{21} + \lambda^2 (b - 3d\lambda^2) I_{22} - 2\lambda (b - 4d\lambda^2) I_{23} + (b - 6d\lambda^2) I_{24} + d I_{25} \quad (\text{A2})$$

$$a_1 = A \left[ B_2 + \frac{\pi R_1^3}{6} (\rho_1 + \rho_2) (1 + 2\xi) - 2\pi\lambda^2 \rho_2 \left\{ R_1 + R_2 + \frac{\pi R_1 R_2}{6} (2\rho_1 R_1^2 + \rho_2 R_2^2) \right\} \right] + (B - C) \frac{\pi}{2} R_1^3 (1 - \xi)^{-4} \quad (\text{A3})$$

$$\lambda = \frac{1}{2} (R_2 - R_1) \quad (\text{A4})$$

$$A = (1 - \xi)^{-3} \quad (\text{A5})$$

$$\xi = \eta_1 R_1^3 + \eta_2 R_2^3 \quad (\text{A6})$$

$$\eta = \frac{\pi \rho_i}{6}, \quad i = 1, 2 \quad (\text{A7})$$

$$B_2 = 1 + \xi + \xi^2 \quad (\text{A8})$$

$$B = B_2 (\rho_1 + \rho_2) \quad (\text{A9})$$

$$C = \frac{72}{\pi} \eta_1 \eta_2 \lambda^2 [R_1 + R_2 + R_1 R_2 (\eta_1 R_1^2 + \eta_2 R_2^2)] \quad (\text{A10})$$

$$I_{21} = I_{23} = -\frac{2R_{21}}{k^2} \cos(kR_{21}) + \frac{2\lambda}{k^2} \cos(k\lambda) + \frac{2}{k^3} \sin(kR_{21}) - \frac{2}{k^3} \sin(k\lambda) \quad (\text{A11})$$

$$I_{22} = -\frac{2}{k^2} [\cos(kR_{21}) - \cos(k\lambda)] \quad (\text{A12})$$

$$I_{24} = -\frac{2R_{21}^2}{k^2} \cos(kR_{21}) + \frac{2\lambda^2}{k^2} \cos(k\lambda) + \frac{4R_{21}}{k^3} \sin(kR_{21}) - \frac{4\lambda}{k^3} \sin(k\lambda) + \frac{4}{k^4} \cos(kR_{21}) - \frac{4}{k^4} \cos(k\lambda) \quad (\text{A13})$$

$$I_{25} = -\frac{2R_{21}^4}{k^2} \cos(kR_{21}) + \frac{2\lambda^4}{k^2} \cos(k\lambda) + \frac{8R_{21}^3}{k^3} \sin(kR_{21}) - \frac{8\lambda^3}{k^3} \sin(k\lambda) + \frac{24R_{21}^2}{k^4} \cos(kR_{21}) - \frac{24\lambda^2}{k^4} \cos(k\lambda) - \frac{48R_{21}}{k^5} \sin(kR_{21}) + \frac{48\lambda}{k^5} \sin(k\lambda) - \frac{48}{k^6} \cos(kR_{21}) + \frac{48}{k^6} \cos(k\lambda) \quad (\text{A14})$$

$$R_{21} = \frac{1}{2} (R_1 + R_2) \quad (\text{A15})$$

$$b = -6R_{21} g_{21} [\eta_1 R_1 g_{11} + \eta_2 R_2 g_{22}] \quad (\text{A16})$$

$$g_{11} = \frac{1}{(1 - \xi)^2} \left[ 1 + \frac{1}{2}\xi + \frac{3}{2}\eta_2 R_2^2 (R_1 - R_2) \right] \quad (\text{A17})$$

$$g_{22} = \frac{1}{(1 - \xi)^2} \left[ 1 + \frac{1}{2}\xi + \frac{3}{2}\eta_1 R_1^2 (R_2 - R_1) \right] \quad (\text{A18})$$

$$g_{21} = \frac{1}{2R_{21}} [R_2 g_{11} + R_1 g_{22}] \quad (\text{A19})$$

$$d = \frac{1}{2} [\eta_1 a_1 + \eta_2 a_2] \quad (\text{A20})$$

$$a_2 = A \left[ B_2 + \frac{\pi R_2^3}{6} (\rho_1 + \rho_2) (1 + 2\xi) - 2\pi\lambda^2 \rho_1 \left\{ R_1 + R_2 + \frac{\pi R_1 R_2}{6} (\rho_1 R_1^2 + 2\rho_2 R_2^2) \right\} \right] + (B - C) \frac{\pi}{2} R_2^3 (1 - \xi)^{-4} \quad (\text{A21})$$

$R_1$  and  $R_2$  are the solvent and solute hard sphere diameters, respectively, and  $\rho_1$  and  $\rho_2$  are the solvent and solute number densities, respectively.

## References and Notes

- (1) Cherayil, B. J.; Fayer, M. D. *J. Chem. Phys.* **1997**, *107*, 7642.
- (2) Oxtoby, D. W. *Annu. Rev. Phys. Chem.* **1981**, *32*, 77.
- (3) Heilweil, E. J.; Casassa, M. P.; Cavanagh, R. R.; Stephenson, J. C. *J. Chem. Phys.* **1986**, *85*, 5004.
- (4) Goodyear, G.; Stratt, R. M. *J. Chem. Phys.* **1997**, *107*, 3098.
- (5) Bakker, H. J. *J. Chem. Phys.* **1993**, *98*, 8496.
- (6) Tokmakoff, A.; Sauter, B.; Fayer, M. D. *J. Chem. Phys.* **1994**, *100*, 9035.
- (7) Myers, D. J.; Shigeiwa, M.; Cherayil, B. J.; Fayer, M. D. *Chem. Phys. Lett.* **1999**, *313*, 592.
- (8) Urdahl, R. S.; Myers, D. J.; Rector, K. D.; Davis, P. H.; Cherayil, B. J.; Fayer, M. D. *J. Chem. Phys.* **1997**, *107*, 3747.
- (9) Myers, D. J.; Shigeiwa, M.; Silbey, R. J.; Fayer, M. D. *Chem. Phys. Lett.* **1999**, *312*, 399.
- (10) Schwarzer, D.; Troe, J.; Zerezke, M. *J. Chem. Phys.* **1997**, *107*, 8380.
- (11) Sun, Y.-P.; Fox, M. A.; Johnston, K. P. *J. Am. Chem. Soc.* **1992**, *114*, 1187.
- (12) Takahashi, K.; Jonah, C. D. *Chem. Phys. Lett.* **1997**, *264*, 297.
- (13) Zhang, J.; Lee, L. L.; Brennecke, J. F. *J. Phys. Chem.* **1995**, *99*, 9268.
- (14) Petsche, I. B.; Debenedetti, P. G. *J. Chem. Phys.* **1989**, *91*, 7075.
- (15) McGuigan, D. B.; Monson, P. A. *Fluid Phase Equilib.* **1990**, *57*, 227.
- (16) Eckert, C. A.; Ziger, D. H.; Johnston, K. P.; Ellison, T. K. *Fluid Phase Equilib.* **1983**, *14*, 167.
- (17) Eckert, C. A.; Ziger, D. H.; Johnston, K. P.; Kim, S. *J. Phys. Chem.* **1986**, *90*, 2738.
- (18) Economou, I. G.; Donohue, M. D. *AIChE J.* **1990**, *36*, 1920.
- (19) Wheeler, J. C. *Ber. Bunsen-Ges. Phys. Chem.* **1972**, *76*, 308.
- (20) Maiwald, M.; Schneider, G. M. *Ber. Bunsen-Ges. Phys. Chem.* **1998**, *102*, 960.
- (21) Sun, Y.-P.; Bunker, C. E. *Ber. Bunsen-Ges. Phys. Chem.* **1995**, *99*, 976.
- (22) Tucker, S. C. *Chem. Rev.* **1999**, *99*, 391.
- (23) Brennecke, J. F.; Tomasko, D. L.; Eckert, C. A. *J. Phys. Chem.* **1990**, *94*, 7692.
- (24) Zagrobelny, J.; Betts, T. A.; Bright, F. V. *J. Am. Chem. Soc.* **1992**, *114*, 5249.
- (25) Zagrobelny, J.; Bright, F. V. *J. Am. Chem. Soc.* **1992**, *114*, 7821.
- (26) Anderton, R. M.; Kauffman, J. F. *J. Phys. Chem.* **1995**, *99*, 13759.
- (27) Heitz, M. P.; Bright, F. V. *J. Phys. Chem.* **1996**, *100*, 6889.
- (28) Heitz, M. P.; Maroncelli, M. *J. Phys. Chem. A* **1997**, *101*, 5852.
- (29) Carlier, C.; Randolph, T. W. *AIChE J.* **1993**, *39*, 876.
- (30) Randolph, T. W.; Carlier, C. *J. Phys. Chem.* **1992**, *96*, 5146.
- (31) Kajimoto, O. *Chem. Rev.* **1999**, *99*, 355.
- (32) Ishii, R.; Okazaki, S.; Okada, I.; Furusaka, M.; Watanabe, N.; Misawa, M.; Fukunaga, T. *Chem. Phys. Lett.* **1995**, *240*, 84.
- (33) Nishikawa, K.; Tanaka, I.; Amemiya, Y. *J. Phys. Chem.* **1996**, *100*, 418.
- (34) Kim, S.; Johnston, K. P. *AIChE J.* **1987**, *33*, 1603.
- (35) Kim, S.; Johnston, K. P. *Ind. Eng. Chem. Res.* **1987**, *26*, 1206.
- (36) Myers, D. J.; Chen, S.; Shigeiwa, M.; Cherayil, B. J.; Fayer, M. D. *J. Chem. Phys.* **1998**, *109*, 5971.
- (37) Goodyear, G.; Tucker, S. C. *J. Chem. Phys.* **1999**, *110*, 3643.
- (38) Yamaguchi, T.; Kimura, Y.; Hirota, N. *J. Chem. Phys.* **1999**, *111*, 4169.
- (39) Tokmakoff, A.; Marshall, C. D.; Fayer, M. D. *J. Opt. Soc. Am. B* **1993**, *10*, 1785.
- (40) Jones, L. H.; McDowell, R. S.; Goldblatt, M. *Inorg. Chem.* **1969**, *8*, 2349.
- (41) Tokmakoff, A.; Urdahl, R. S.; Zimdars, D.; Francis, R. S.; Kwok, A. S.; Fayer, M. D. *J. Chem. Phys.* **1995**, *102*, 3919.
- (42) Myers, D. J.; Shigeiwa, M.; Silbey, R.; Fayer, M. D. In progress.
- (43) Bader, J. S.; Berne, B. J. *J. Chem. Phys.* **1994**, *100*, 8359.
- (44) Egorov, S. A.; Everitt, K. F.; Skinner, J. L., *J. Phys. Chem. A* **1999**, *103*, 9494.
- (45) Lebowitz, J. L. *Phys. Rev.* **1964**, *133*, 895.
- (46) Stanley, H. E. *Introduction to Phase Transitions and Critical Phenomena*; Oxford: New York, 1971.
- (47) Kawasaki, K. *Ann. Phys.* **1970**, *61*, 1.
- (48) Postol, T. A.; Pelizzari, C. A. *Phys. Rev. A* **1978**, *18*, 2321.
- (49) de Schepper, I. M.; Verkerk, P.; van Well, A. A.; de Graaf, L. A. *Phys. Rev. Lett.* **1983**, *50*, 974.
- (50) Bafille, U.; Verkerk, P.; Barocchi, F.; de Graaf, L. A.; Suck, J.-B.;



- Mutka, H. *Phys. Rev. Lett.* **1990**, *65*, 2394.
- (51) de Schepper, I. M.; Cohen, E. G. D. *Phys. Rev. A* **1980**, *22*, 287.
- (52) Alley, W. E.; Alder, B. J.; Yip, S. *Phys. Rev. A* **1983**, *27*, 3174.
- (53) Alley, W. E.; Alder, B. J. *Phys. Rev. A* **1983**, *27*, 3158.
- (54) de Schepper, I. M.; van Rijs, J. C.; van Well, A. A.; Verkerk, P.; de Graaf, L. A. *Phys. Rev. A* **1984**, *29*, 1602.
- (55) Egelstaff, P. A. *Adv. Phys.* **1962**, *11*, 203.
- (56) Egorov, S. A.; Skinner, J. L. *J. Chem. Phys.* **1996**, *105*, 7047.
- (57) Younglove, B. A.; Ely, J. F. *J. Phys. Chem. Ref. Data* **1987**, *16*, 543.
- (58) Friend, D. G.; Ingham, H.; Ely, J. F. *J. Phys. Chem. Ref. Data* **1991**, *20*, 275.
- (59) Standards, N. I. o. *NIST Standard Reference Database 14*, 9.08 ed.; U.S. Department of Commerce: Boulder, CO, 1992.
- (60) Rubio, R. G.; Zollweg, J. A.; Streett, W. B. *Ber. Bunsen-Ges. Phys. Chem.* **1989**, *93*, 791.
- (61) Altunin, V. V. *Thermophysical properties of Freons: methane series*; Hemisphere Publishing Company: Washington, DC, 1987.
- (62) *Thermophysical Properties of Refrigerants*; Platzer, B., Polt, A., Maurer, G., Eds.; Springer-Verlag: Berlin, 1990; Vol. VII.
- (63) Kenkre, V. M.; Tokmakoff, A.; Fayer, M. D. *J. Chem. Phys.* **1994**, *101*, 10618.
- (64) Heinemann, F.; Schmidt, H.; Peters, K.; Thiery, D. *Z. Kristallogr.* **1992**, *198*, 123.
- (65) Ben-Amotz, D.; Herschbach, D. R. *J. Phys. Chem.* **1990**, *94*, 1038.
- (66) Torrie, B. H.; Binbrek, O. S.; Powell, B. M. *Mol. Phys.* **1996**, *87*, 1007.
- (67) Moore, P.; Tokmakoff, A.; Keyes, T.; Fayer, M. D. *J. Chem. Phys.* **1995**, *103*, 3325.
- (68) Moore, P. B.; Ji, X.; Ahlborn, H.; Space, B. *Chem. Phys. Lett.* **1998**, *296*, 259.
- (69) Vijayadamodar, G. V.; Nitzan, A. *J. Chem. Phys.* **1995**, *103*, 2169.
- (70) Ishii, R.; Okazaki, S.; Okada, I.; Furusaka, M.; Watanabe, N.; Misawa, M.; Fukunaga, T. *J. Chem. Phys.* **1996**, *105*, 7011.
- (71) Egorov, S. A.; Skinner, J. L. *J. Chem. Phys.*, in press.
- (72) Egorov, S. A.; Skinner, J. L. *J. Chem. Phys.* **2000**, *112*, 275.
- (73) Blitz, J. P.; Yonker, C. R.; Smith, R. D. *J. Phys. Chem.* **1989**, *93*, 6661.
- (74) Pan, X.; McDonald, J. C.; MacPhail, R. A. *J. Chem. Phys.* **1999**, *110*, 1677.